

Single-Photon Source Over the Terahertz Regime

Caspar Groiseau[✉], * Antonio I. Fernández-Domínguez, Diego Martín-Cano,[†] and Carlos Sánchez Muñoz^{✉‡}

Departamento de Física Teórica de la Materia Condensada and Condensed Matter Physics Center (IFIMAC), Universidad Autónoma de Madrid, Madrid 28049, Spain



(Received 30 May 2023; revised 19 October 2023; accepted 5 December 2023; published 29 January 2024)

We present a proposal for a tunable source of single photons operating in the terahertz (THz) regime. This scheme transforms incident visible photons into quantum THz radiation by driving a single polar quantum emitter with an optical laser, with its permanent dipole enabling dressed THz transitions enhanced by the resonant coupling to a cavity. This mechanism offers optical tunability of properties such as the frequency of the emission or its quantum statistics (ranging from antibunching to entangled multiphoton states) by modifying the intensity and frequency of the drive. We show that the implementation of this proposal is feasible with state-of-the-art photonics technology.

DOI: 10.1103/PRXQuantum.5.010312

I. INTRODUCTION

Terahertz (THz) radiation—lying at frequencies from 0.1 THz to 70 THz—has sparked broad interest recently [1,2] due to its key relevance for addressing transition frequencies of vibrational and rotational levels in molecules [3], as well as single-particle and collective transitions in semiconductor materials [4]. Such potential provides an avenue to harness light-matter interactions with relevant applications (primarily related to imaging and spectroscopy) in multiple areas, ranging from food sciences [5], medical diagnostics, and biology [6] to high-bandwidth communication [7] or security [8].

However, quantum THz technology is at a much more incipient stage than its visible, near-infrared, or microwave counterparts [9–11]. As already demonstrated in these spectral regimes, quantum light offers important technological advantages, such as metrological precision at the Heisenberg limit [12], alternative quantum computing paradigms [13], or eavesdropping protection in remote communications [14]. Through the development of THz quantum technology, these advances could be transferred and exploited in areas where THz radiation is of key relevance. This avenue would also mean an opportunity to reduce the experimental requirements inherent in

current quantum optical implementations, since THz quantum platforms are expected to offer a compromise between the microwave regime, which demands cooling down to millikelvin temperatures and involve important scalability challenges, and the optical one, where materials are strongly absorptive and require nanometric precision in fabrication. The common mechanism of deterministic single-photon emission enabled by optical dipole transitions in quantum emitters is drastically limited, if not absent, in the THz regime, because the electronic pure dephasing is orders of magnitude larger than the THz emission rate [15]. There are, however, a few demonstrations of heralded quantum THz radiation sources based on spontaneous parametric down-conversion [16].

A promising route toward the emission of THz radiation is to exploit the dressing between electronic transitions and driving electric fields, i.e., the ac or dynamical Stark effect. This dressing splits the energy levels into doublets separated by the Rabi frequency Ω_R [see Fig. 1(a)], which for certain values of the field intensity can lie in the THz regime. Crucially, in polar systems with broken inversion symmetry, radiative transitions among dressed states in the same Rabi doublet become dipole allowed and have been proposed as a possible channel of emission of THz radiation [17–22]. However, to the best of our knowledge, only classical properties of the THz radiation generated—such as the emission spectrum—or semiclassical lasing limits have been considered in such systems. Experimental evidence for such transitions enabled by permanent dipoles exists for Rabi splitting of the order of gigahertz in superconducting qubits [23].

In this work, we show the prospects of this mechanism with single polar emitters for the realization of quantum optics in the THz regime, demonstrating its ability for the

*caspar.groiseau@uam.es

†diego.martin.cano@uam.es

‡carlos.sanchezmunoz@uam.es

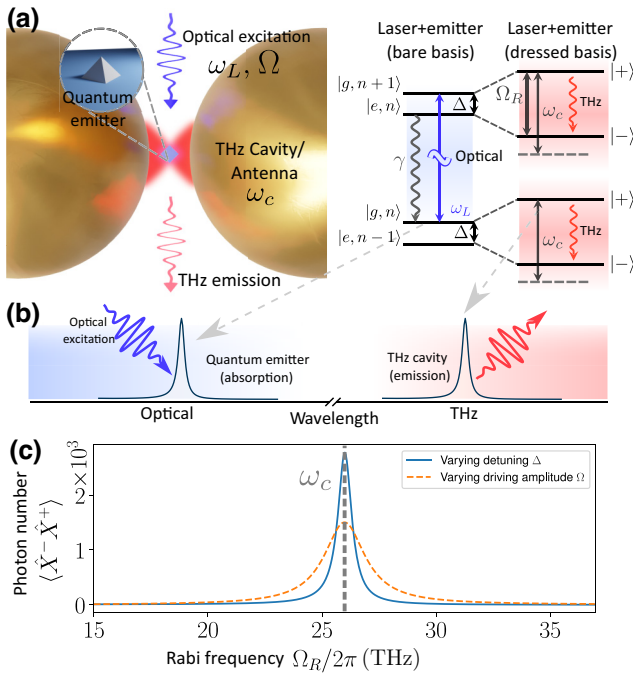


FIG. 1. (a) A sketch of a potential experimental implementation with a quantum emitter trapped in a cavity made up by two nanospheres (left) and the energy-level structure (right): the left part represents the bare-states basis, highlighting energy differences in the optical domain (blue); the right side represents the dressed-state basis, highlighting THz transitions (red). (b) The absorption and emission properties in the THz and the optical domain. (c) The resonance in the cavity population as the Rabi frequency crosses the cavity frequency for $\{\chi, \kappa, \gamma, \omega_c\}/2\pi = \{0.05, 0.158, 0.0005, 26\}$ THz. Ω_R is swept while fixing either the laser amplitude $\Omega/2\pi = 10$ THz (blue solid line) or the detuning $\Delta/2\pi = 10$ THz (orange dashed line).

transduction of classical visible light into THz radiation with diverse purely quantum properties, such as single-photon emission, multiphoton emission, and nonclassical correlations between different frequencies of emission. We consider that the single polar emitter is dressed by an optical laser and that its resulting THz transitions—enabled between the two states of a Rabi doublet—couple to a THz nanophotonic cavity. The cavity provides a Purcell enhancement of the emission that is eventually radiated into free space. This design exploits the tunability of the laser parameters and the THz nanocavity architecture to provide considerable brightness and remarkable optical control of the quantum properties of the emission.

II. MODEL

We consider a single two-level system (TLS), consisting of a ground state $|g\rangle$ and an excited state $|e\rangle$, separated by the optical transition frequency ω_0 . The TLS is driven by a laser field \mathbf{E}_L of frequency ω_L , which is also in the optical range. Furthermore, the TLS couples

to a single-cavity mode (annihilation operator \hat{a}) with the THz frequency ω_c and field \mathbf{E}_c [for a schematic representation, see Fig. 1(a)]. These features are described by the Hamiltonian ($\hbar = 1$): $\hat{H} = \omega_0 \hat{\sigma}_z / 2 + \omega_c \hat{a}^\dagger \hat{a} + \hat{\mathbf{d}} \cdot \mathbf{E}_c (\hat{a} + \hat{a}^\dagger) + \hat{\mathbf{d}} \cdot \mathbf{E}_L \cos(\omega_L t)$, where we have defined the dipole operator $\hat{\mathbf{d}} = \mathbf{d}_{ee}(1 + \hat{\sigma}_z)/2 + \mathbf{d}_{ge}(\hat{\sigma}_+ + \hat{\sigma}_-)$, with $\hat{\sigma}_{\pm z}$ being the Pauli matrices of the TLS. The term $\propto \mathbf{d}_{ee}$ describes the permanent dipole component, originating from asymmetries in the charge distribution of its ground state.

The coherent drive gives rise to two dressed eigenstates of the quantum emitter-laser subsystem, split in energy by the Rabi frequency $\Omega_R = \sqrt{\Delta^2 + \Omega^2}$, where $\Delta = \omega_L - \omega_0$ and $\Omega = \mathbf{d}_{ge} \cdot \mathbf{E}_L$ are the laser detuning and the driving amplitude, respectively [20,24]. These states are given by $|+\rangle = s|e\rangle + c|g\rangle$ and $|-\rangle = -c|e\rangle + s|g\rangle$, where we define $s = \sin \theta$, $c = \cos \theta$, with $\theta \equiv \arctan(h) \in [0, \pi/4]$, and h is a dressing ratio, defined as $h \equiv (\Omega_R - \Delta)/\Omega \in [0, 1]$ that identifies the limit of no dressing ($h = 0$) and the resonant limit of a fully dressed emitter ($h = 1$). The $\hat{\sigma}_{\pm z}$ operators can be expressed straightforwardly in terms of the Pauli matrices of the dressed-state basis $\hat{\xi}_{\pm z}$, i.e., $\hat{\sigma}_\pm = cs\hat{\xi}_z + s^2\hat{\xi}_\pm - c^2\hat{\xi}_\mp$ and $\hat{\sigma}_z = (s^2 - c^2)\hat{\xi}_z - 2cs(\hat{\xi}_+ + \hat{\xi}_-)$. By applying a rotating-wave approximation to eliminate all terms oscillating at optical frequencies in \hat{H} and then moving to the dressed basis by writing the TLS operators in terms of $\hat{\xi}_{\pm z}$, we obtain the following Hamiltonian [20]:

$$\begin{aligned} \hat{H} = & \frac{\Omega_R}{2} \hat{\xi}_z + \omega_c \hat{a}^\dagger \hat{a} - 2cs\chi(\hat{a}\hat{\xi}_+ + \hat{a}^\dagger\hat{\xi}_-) \\ & - 2cs\chi(\hat{a}\hat{\xi}_- + \hat{a}^\dagger\hat{\xi}_+) + \chi(\hat{a} + \hat{a}^\dagger)[1 + (s^2 - c^2)\hat{\xi}_z]. \end{aligned} \quad (1)$$

Here, $\chi = \mathbf{d}_{ee} \cdot \mathbf{E}_c / 2$ is the coupling rate between the TLS and the THz cavity, which, importantly, depends on the permanent component of the dipole moment. This permanent dipole moment allows for cavity-emitter coupling terms of the form $\propto (\hat{a} + \hat{a}^\dagger)\hat{\sigma}_z$ in the original Hamiltonian, which, crucially, oscillate at THz frequencies, enabling resonant interactions between the THz cavity and the dressed emitter.

Additionally, we take into account cavity photon loss with a rate κ and TLS excitation decay with the spontaneous emission rate in vacuum γ . The presence of counter-rotating terms in Eq. (1) requires a careful description of the interaction between the system and the bath to prevent unphysical processes such as the emission of photons at zero frequency. In particular, these terms induce a change in the time dependence of the field operator ($\hat{a}(t) \neq \hat{a}(0)e^{-i\omega ct}$), which affects the typical secular approximation commonly made during the derivation of the master equation in the optical regime (similar to the situation found in the ultrastrong-coupling regime [25–27]). As a result, the interaction between the cavity

and the environment is described by the operator $\hat{X}^+ = \sum_{j,k>j} \sqrt{\omega_{kj}/\omega_c} |j\rangle\langle(\hat{a} + \hat{a}^\dagger)|k\rangle\langle j|\langle k|$ that encompasses all the positive-frequency transitions of $(\hat{a} + \hat{a}^\dagger)$ [28]. Here, $|k\rangle$ is the k th eigenstate with energy ω_k (sorted in ascending order) and $\omega_{kj} = \omega_k - \omega_j$. The scaling of \hat{X}^+ with ω_{kj} is chosen to describe the coupling to an Ohmic bath [26]. We also define $[\hat{X}^+]^\dagger = \hat{X}^-$. The complete dynamics of the open quantum system are thus described by the master equation [29], $\dot{\rho} = -i[\hat{H}, \rho] + \gamma/(2)\mathcal{D}(\hat{\sigma}_-) + \kappa/(2)\mathcal{D}(\hat{X}^+)$, where we have defined the Lindblad superoperator $\mathcal{D}(\hat{O}) = 2\hat{O}\hat{\rho}\hat{O}^\dagger - \hat{O}^\dagger\hat{O}\hat{\rho} - \hat{\rho}\hat{O}^\dagger\hat{O}$ and where the usual decay term $\mathcal{D}(\hat{a})$ has been replaced by $\mathcal{D}(\hat{X}^+)$ [30]. Similarly, the input-output relations are given by $\hat{a}_{\text{out}} = \hat{a}_{\text{in}} + \sqrt{\kappa}\hat{X}^+$ [31], so that quantities such as the radiated photon flux will be given by $\kappa\langle\hat{X}^-\hat{X}^+\rangle$. For the case of the emitter, the dressed operator for spontaneous emission remains identical to $\hat{\sigma}_-$.

In practice, we observe that the standard Lindblad description with $\mathcal{D}(\hat{a})$ gives qualitatively the same results as using $\mathcal{D}(\hat{X}^+)$, given that we are far from being in the ultrastrong-coupling limit ($\chi \ll \omega_c$). On the other hand, the use of the proper input-output relations in terms of \hat{X}^\pm is crucial, since otherwise one would describe the unphysical emission of photons with energies equal or close to zero. Even in cases in which these photons only make a minor contribution to the total photon flux emitted, they have a significant impact on the photon statistics, leading to important incorrect contributions to bunched photon statistics when $\Omega_R < \omega_c$ (see Appendix A).

To gain a better understanding of the dynamics, it is helpful to express the dissipative part in terms of the dressed TLS operators $\hat{\zeta}_{\pm,z}$. After discarding off-resonant terms based on the assumption that $\omega_c \gg \gamma$, one obtains a combination of effective incoherent losses, pumping, and dephasing, $\dot{\rho} = -i[\hat{H}, \rho] + \gamma_-/(2)\mathcal{D}(\hat{\zeta}_-) + \gamma_+/(2)\mathcal{D}(\hat{\zeta}_+) + \gamma_z/(2)\mathcal{D}(\hat{\zeta}_z) + \kappa/(2)\mathcal{D}(\hat{X}^+)$, that all depend on the laser detuning, i.e., $\gamma_- = \gamma s^4$, $\gamma_+ = \gamma c^4$, and $\gamma_z = \gamma c^2 s^2$. It can be shown that this configuration drives the dressed-state population inversion ($\gamma_+ > \gamma_-$), if the laser is blue-detuned $\Delta > 0$ [20], which is the setting that we will choose for the rest of the paper. In order to achieve a high emission flux, a limit of interest is that of a saturated dressed emitter, reached when the pumping rate greatly exceeds its decay, $\gamma_+ \gg \gamma_-$. This situation takes place when the driving detuning is much larger than the Rabi-doublet splitting ($\Delta \gg \Omega$), corresponding to a small dressing ratio $h \ll 1$.

III. RESONANT MECHANISM OF THz EMISSION

By tuning the Rabi frequency Ω_R in resonance with the cavity frequency, ω_c , Jaynes-Cummings-like terms $\propto \hat{a}\hat{\zeta}_+ + \hat{a}^\dagger\hat{\zeta}_-$ in Eq. (1) become resonant and dominate the dynamics. In this regime, the system becomes

efficient at absorbing optical radiation from the driving field and emitting THz photons, since intradoublet THz transitions are Purcell enhanced by the cavity. This regime of operation is sketched in Fig. 1(b) and demonstrated in Fig. 1(c), which shows the substantial increase in the cavity population when Ω_R is tuned into this resonant regime. Around this point of operation, we can ignore off-resonant terms in Eq. (1) (provided that $\omega_c \gg \chi$) and use the resulting effective Jaynes-Cummings Hamiltonian for the dressed states $\hat{H} = \Omega_R\hat{\zeta}_z/2 + \omega_c\hat{a}^\dagger\hat{a} - 2cs\chi(\hat{a}\hat{\zeta}_+ + \hat{a}^\dagger\hat{\zeta}_-)$. Since under this approximation we have neglected counter-rotating terms, we can safely substitute \hat{X}^+ by \hat{a} in the Lindblad term of the master equation and in the calculations of photon flux. This substitution enables us to obtain approximate analytical solutions, which provide valuable insights into the different emission regimes.

For this analytical calculation, we can assume that the cavity is nearly empty and treat it as a TLS (truncating the number of excitations at 1). Then, we obtain that the photon flux in the resonant condition ($\Omega_R = \omega_c$) is given by

$$\kappa\langle\hat{a}^\dagger\hat{a}\rangle = \frac{\kappa}{\tilde{\kappa}} \left(\frac{\gamma_+}{1 + \tilde{C}^{-1} - 4\gamma_z/\tilde{\kappa}} \right), \quad (2)$$

where we have introduced the effective cooperativity $\tilde{C} \equiv 16\chi^2/\kappa\gamma(h^2 + h^{-2})^{-1}$ and an effective rate $\tilde{\kappa} \equiv \gamma_+ + \gamma_- + 4\gamma_z + \kappa$. The full expression as a function of ω_c , which can be found in Appendix B, describes a Lorentzian centered around Ω_R , as shown in Fig. 1(c).

Note that the introduced effective cooperativity \tilde{C} is closely connected to the standard expression of the cooperativity, $C = 4\chi^2/\kappa\gamma$, but accounts for the effective coupling between the cavity and the dressed emitter, which depends on the detuning between emitter and drive via h , so that $\tilde{C} = 4C/(h^2 + h^{-2})$. In the strongly detuned case $h \ll 1$, we have $\tilde{C} \approx 4Ch^2$. To provide an understanding of the relationship between these quantities, note that a typical value of h for the parameters chosen in the text is $h \approx 0.2$, meaning that $\tilde{C} \approx 0.16C$. A natural limit to consider is when cavity losses represent the dominant decay channel, $\kappa \gg \gamma$, which implies that $\tilde{\kappa} \approx \kappa$. In that case, in the limit of small cooperativity, $\tilde{C} \ll 1$, the photon flux acquires the simple form $\kappa\langle\hat{a}^\dagger\hat{a}\rangle \approx \gamma_+\tilde{C}$, meaning that the flux will increase as κ is decreased (so that \tilde{C} is increased). On the other hand, if the cooperativity is large $\tilde{C} \gg 1$, we find that $\kappa\langle\hat{a}^\dagger\hat{a}\rangle \approx \gamma_+$. The flux reaches a maximum value when κ is decreased into the strong-coupling region $\kappa = 4cs\chi$, an exact value that we obtain by optimizing Eq. (2). This maximum flux is, again, simply given by $\kappa\langle\hat{a}^\dagger\hat{a}\rangle \approx \gamma_+$ in the natural situation of $\gamma \ll \chi$ and detuned driving, $h \ll 1$. The fact that the maximum photon flux is given by γ_+ implies that the brightness of the THz source scales with the *optical* emission rate into free space.

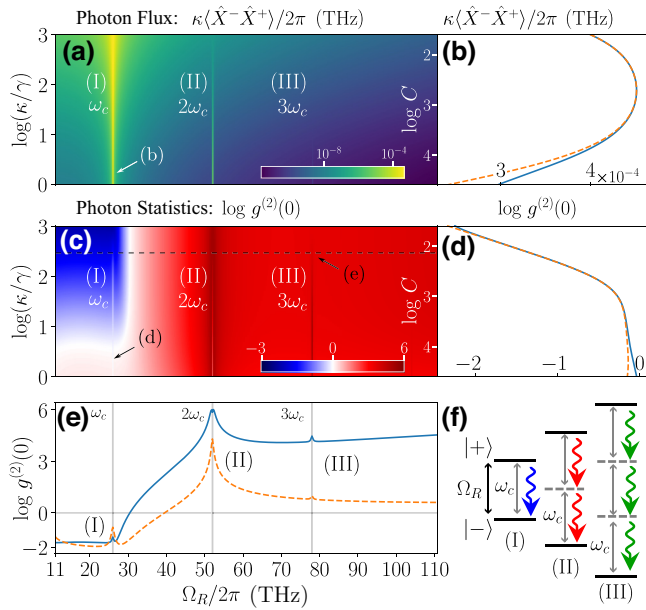


FIG. 2. (a) A map of the output photon flux $\kappa\langle\hat{X}^-\hat{X}^+\rangle$ as a function of Ω_R for $\{\chi, \gamma, \omega_c\}/2\pi = \{0.05, 0.0005, 26\}$ THz and fixed $\Omega/2\pi = 10$ THz. (b) A cut of (a) for fixed $\Omega_R = \omega_c$, showing both a numerical calculation of $\kappa\langle\hat{X}^-\hat{X}^+\rangle$ (blue solid line) and the analytical solution for $\kappa\langle\hat{a}^\dagger\hat{a}\rangle$ (orange dashed line) in the Jaynes-Cummings approximation. The same (c) map and (d) cut, for the degree of quantum second-order coherence $g^{(2)}(0) = \langle\hat{X}^-\hat{X}^-\hat{X}^+\hat{X}^+\rangle/\langle\hat{X}^-\hat{X}^+\rangle^2$, with (d) showing results from the simulations (blue solid line) and from the analytics (orange dashed line). The value of κ/γ chosen for the plot in (e) is marked by the dashed horizontal line. (e) $g^{(2)}(0)$ versus Ω_R with $\log(\kappa/\gamma) = 2.5$. Ω_R is changed in two ways: varying Δ (blue solid line) and varying Ω with fixed $\Delta/2\pi = 10$ THz (orange dashed line). (f) A sketch of the main processes taking place at specific resonances in the maps.

This relationship is noteworthy because the optical emission rate is significantly larger than its THz counterpart, since both scale with the emission frequency as ω^3 . A more detailed analytical study of the conditions of maximum flux, including a full expression valid for all regimes, is provided in Appendix B. If κ is further decreased to the point at which $\kappa \gg \gamma$, the photon flux gets reduced below its maximum value of γ_+ , since $\tilde{\kappa} \not\approx \kappa$. We then conclude that the regime of operation that provides the highest possible photon flux of γ_+ is given by the conditions $\kappa \gg \gamma$ and $\tilde{C} \gg 1$. We note that this last condition implies a more complex relationship between Ω and γ than the usual strong-coupling condition $\Omega \gg \gamma$. In particular, we can express $\tilde{C} \gg 1$ (while still assuming $h \ll 1$) as $\Omega \gg \Omega_R/\sqrt{C}$, which relates the required driving amplitude to not only γ but also χ and κ . Nevertheless, this condition will normally imply pump powers compatible with the strong-coupling regime. This is indeed the case for the small values of γ considered here. We provide

estimations and simulations of experimentally achievable Ω in Appendix C.

These analytical estimations are confirmed by exact numerical results. Figure 2(a) shows exact calculations of the output photon flux $\kappa\langle\hat{X}^-\hat{X}^+\rangle$ as a function of κ/γ and Ω_R . On the other hand, Fig. 2(b) shows the flux at the resonance $\Omega_R = \omega_c$ [labeled (I)] versus κ/γ . In both plots, Ω_R is modified by fixing Ω and varying the detuning Δ . The orange line in Fig. 1(b) corresponds to the analytical formula in Eq. (2), confirming the validity of our analytical results.

Next, we consider the quantum statistics of the emission, measured through the zero-delay second-order correlation function $g^{(2)}(0) = \langle\hat{X}^-\hat{X}^-\hat{X}^+\hat{X}^+\rangle/\langle\hat{X}^-\hat{X}^+\rangle^2$. We show numerical calculations of its steady-state value in Figs. 2(c) and 2(d). Notably, we find that the resonance (I) coincides with a regime of strongly antibunched emission where $g^{(2)}(0) < 1$, meaning that, in the regime in which the output flux is maximum, *this platform operates as a single THz photon source*. By truncating at two excitations, we can obtain an analytical expression for $g^{(2)}(0)$ (for a general expression and further details, see Appendix B). $g^{(2)}(0)$ is antibunched for $\kappa > \gamma$ but when κ is decreased into the strong-coupling regime, most of the antibunching will be lost as the system undergoes a lasing phase transition [see the kink in the curve in Fig. 2(d), after which $g^{(2)}(0)$ slowly trends toward 1, i.e., a coherent state]. Note that at resonance ($\Omega_R = \omega_c$), there is a small region of near-coherent states within the antibunched region, meaning that the antibunching can be made much stronger by setting the cavity slightly out of this resonance. This effect is more important the lower the κ and is more visible in the Ω ramp in Fig. 8 in Appendix D.

IV. MULTIPHOTON RESONANCES

Beyond the main resonant mechanism of THz photon emission at $\Omega_R = \omega_c$ described so far, a sweep over the Rabi frequency such as the one shown in Figs. 2(a), 2(c), and 2(e) also unveils additional features in both the output flux and the emission statistics. In particular, one can observe small peaks in the output photon flux when the Rabi frequency Ω_R is exactly twice (II) or three times (III) the cavity frequency ω_c (the latter case is barely visible). These peaks are related to multiphoton processes enabled by the counter-rotating terms of the form $\hat{\xi}_+\hat{a}^\dagger$ and $\hat{\xi}_z\hat{a}^\dagger$ in Eq. (1), which we have ignored in our analytical derivations presented above. Each peak corresponds to an n th-order process becoming resonant, as has been previously reported in other light-matter systems featuring interaction terms that do not conserve either parity or the total number of excitations [32–34]. Indeed, at these points, the dynamics are governed by an effective n th-order Hamiltonian $\hat{H}_{\text{eff}} = \lambda_n \left[(\hat{a})^n \hat{\xi}_+ + (\hat{a}^\dagger)^n \hat{\xi}_- \right]$, where $n = 2$

or 3 for (II) and (III), respectively (further information, with analytical expressions for λ_n , can be found in Appendix E). In the presence of dissipation, this gives rise to strongly correlated emission, which in our case corresponds to the simultaneous emission of multiple photons within a Rabi doublet [see Fig. 2(f)]. The activation of each of these resonances results in an extraordinary degree of optical tunability of the quantum statistics of the emission, as seen Fig. 2(e), where, by changing the Rabi frequency of the drive Ω_R , $g^{(2)}(0)$ spans 8 orders of magnitude from antibunching to superbunching.

The tunability offered when the Rabi frequency Ω_R is alternatively modified by optically tuning the laser power Ω instead of its detuning is very similar [cf. the dashed orange line in Fig. 2(e)]. However, the limits of c and s are inverted, which leads to bunching for low Ω and coherent states for large Ω (further details on the two tuning methods can be found in Appendix D). Overall, we find that modifying Δ is a more versatile way to control the system, since the use of strong driving to reach high values of Ω_R can result in added pure dephasing.

V. SPECTRAL FEATURES

Beyond the demonstrated tunability of photon statistics, our proposal can also deliver broadband control over the emission frequency, oftentimes a limiting factor in sources of THz radiation. To showcase this feature, we ramp Ω_R and record the cavity emission spectrum $S_\Gamma(\omega) = 1/\pi \int_0^\infty e^{i(\omega-\Gamma/2)\tau} \langle \hat{X}^-(0) \hat{X}^+(\tau) \rangle d\tau$, where Γ is the bandwidth of the sensor, which we take to be equal to κ . We focus on a particular case where $\kappa = 0.158$ THz, since that value exhibits both strong antibunching and a large output photon flux [see Figs. 2(b) and 2(d)]. The main frequency of emission is set by the dressed emitter and equal to Ω_R . This feature can be clearly seen in Fig. 3(a), which shows $S_\Gamma(\omega)$ as the Rabi frequency Ω_R is varied. This indicates that the Jaynes-Cummings type of dynamics characteristic of the resonance (I) remains important even out of resonance.

A strong secondary signal in the spectrum is observed at the cavity frequency ω_c , regardless of the value of Ω_R . Finally, when $\Omega_R > \omega_c$, a third peak also emerges at a frequency $\omega_2 = \Omega_R - \omega_c$, which is a signature of a two-photon processes in which the deexcitation of the dressed emitter within a Rabi doublet is accompanied by the emission of a photon at the cavity frequency ω_c and a second photon of frequency ω_2 , matching the energy-conservation condition $\omega_c + \omega_2 = \Omega_R$. This observation suggests nontrivial dynamics of emission of multimode correlated states, which should manifest as strong features of the frequency-resolved second-order correlation function at zero delay, $g_\Gamma^{(2)}(\omega_1, \omega_2)$ [35–37]. To confirm this, we resort to the sensor method developed in Ref. [35] and compute this quantity through the correlations between

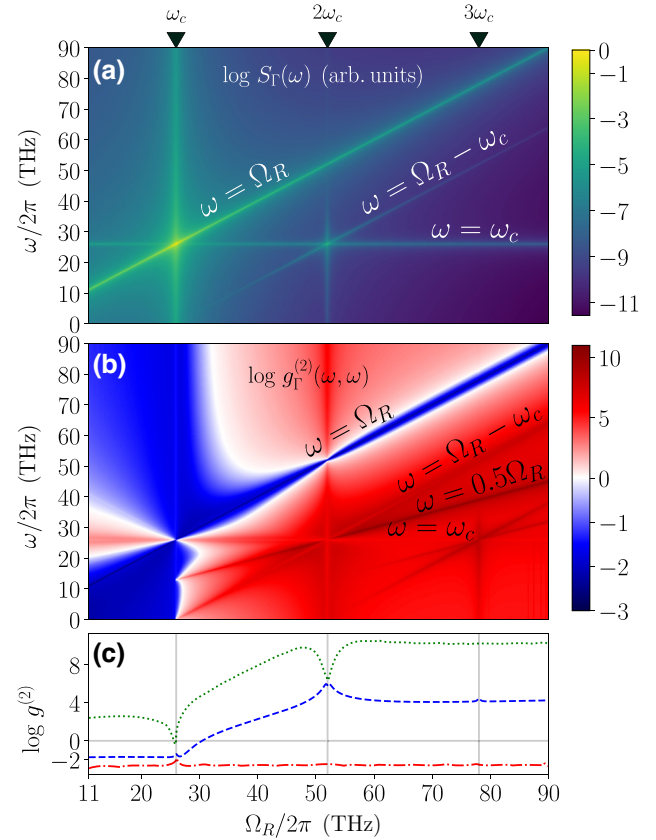


FIG. 3. Maps of (a) the spectrum $S_\Gamma(\omega)$ [shown as $\log S_\Gamma(\omega)$ (in arbitrary units)] and (b) the degree of quantum second-order coherence $g_\Gamma^{(2)}(\omega, \omega)$ [shown as $\log g_\Gamma^{(2)}(\omega, \omega)$] as a function of ω and Ω_R for $\{\chi, \kappa, \gamma, \omega_c\}/2\pi = \{0.05, 0.158, 0.0005, 26\}$ THz. We highlight some of the lines in the maps and denote the corresponding photon frequencies (black). (c) $g^{(2)}(0)$ [shown as $\log g^{(2)}(0)$] (blue dashed line), $\max_\omega g_\Gamma^{(2)}(\omega, \omega)$ [shown as $\log[\max_\omega g_\Gamma^{(2)}(\omega, \omega)]$] (green dotted line), and $\min_\omega g_\Gamma^{(2)}(\omega, \omega)$ [shown as $\log[\min_\omega g_\Gamma^{(2)}(\omega, \omega)]$] (red dash-dotted line) for fixed $\Omega/2\pi = 10$ THz.

two ancillary qubits, fixing the spectral resolution of these sensors equal to the cavity line width $\Gamma = \kappa$ (see Appendix F). We first compute the photon statistics for a given spectral frequency ω , i.e., $g_\Gamma^{(2)}(\omega, \omega)$, versus Ω_R , as shown in Fig. 3(b). We observe that the main emission line $\omega = \Omega_R$ is strongly antibunched, as expected since emission at this frequency stems from first-order processes originating from Jaynes-Cummings-like interaction terms. The other two lines that are clearly visible in the spectrum feature bunched statistics, evidencing their multiphoton character, and a new strongly bunched line at $\omega = \Omega_R/2$, not visible in the spectrum, is also present. This line corresponds to two-photon processes in which both photons are emitted at the same frequency (instead of one of them being emitted at the cavity frequency). Since this process is not stimulated by the cavity, it is only visible in the statistics.

These results suggest that frequency filtering can act as an extra control knob of the quantum statistics of the THz emission. Indeed, this is illustrated in Fig. 3(c), where we plot the minimum and maximum possible values of $g_{\Gamma}^{(2)}(\omega, \omega)$ over ω for each Ω_R , which ends up always being, respectively, lower or larger than the degree of coherence of the unfiltered signal, $g_{\Gamma}^{(2)}(0)$. The large difference between these maximum and minimum values of $g_{\Gamma}^{(2)}(\omega, \omega)$ highlights the tunability offered by the method of frequency filtering in the THz regime.

Beyond the obvious potential of antibunched THz sources for quantum technologies, spectrally correlated emission such as the type we are reporting also holds the potential of quantum applications exploiting non-classical properties such as entanglement [38,39]. To reveal potential nonclassical correlations, we inspect the cross-correlations between two different frequencies, ω_1 and ω_2 . Correlations with nonclassical character can be identified by the violation of the Cauchy-Schwarz inequality (CSI), reformulated as $R(\omega_1, \omega_2) = [g_{\Gamma}^{(2)}(\omega_1, \omega_2)]^2 / [g_{\Gamma}^{(2)}(\omega_1, \omega_1)g_{\Gamma}^{(2)}(\omega_2, \omega_2)] \leq 1$ [40–42]. Figure 4 shows a typical map of $R(\omega_1, \omega_2)$ in frequency-frequency space, where we chose a relatively large Rabi splitting $\Omega_R/2\pi = 70$ THz that allows for multiphoton processes to be observable. This map presents a plethora of features that evidence the richness and complexity of the different quantum processes of emission present in this THz source. Providing a complete catalog of these features is beyond the scope of this paper. However, we highlight that the dominant feature exhibiting a strong violation of the CSI is the antidiagonal line described by the equation $\omega_1 + \omega_2 = \Omega_R$, corresponding to the joint emission of two photons by the deexcitation of the emitter within a Rabi doublet. For this line, one would also find a violation of the Clauser-Horne-Shimony-Holt inequality [41,43] (result not shown). In summary, our results suggest that this source can emit entangled THz photon pairs via two-photon processes. Furthermore, we note that our observation of the two-photon resonant peak (II) in the output flux, corresponding to the case $\omega_1 = \omega_2 = \omega_c$, evidences that these processes can be Purcell enhanced by a cavity in a mechanism akin to previous reports of bundle emission [44].

VI. EXPERIMENTAL FEASIBILITY

We now discuss the experimental viability of the single-photon THz sources proposed in this work. First, we show that the particular set of parameters considered for the calculations in this paper, $\{\chi, \kappa\}/2\pi = \{0.05, 0.158\}$ THz, is readily accessible across a range of platforms. The coupling rate χ is set by the static dipole moment \mathbf{d}_{ee} and the electric field strength at the location of the emitter. We consider a value $|\mathbf{d}_{ee}| = 50$ D as reported in colloidal quantum dots [45], which are known for their

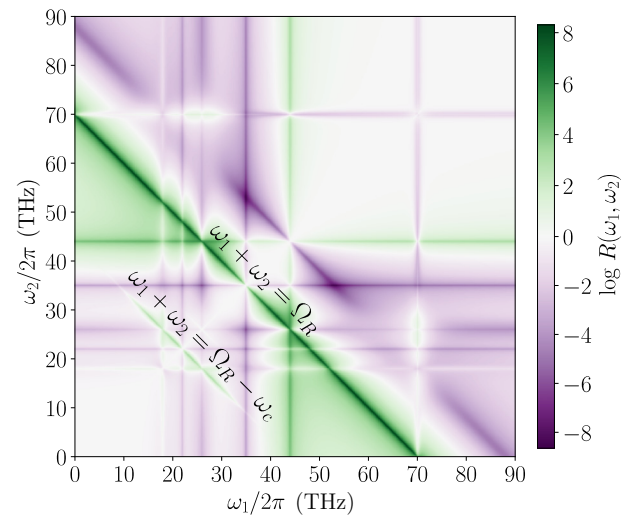


FIG. 4. A map of the violation of the Cauchy-Schwarz inequality via frequency-resolved correlations [shown as $\log R(\omega_1, \omega_2)$]. The parameters used are $\{\chi, \kappa, \gamma, \omega_c, \Omega_R, \Omega\}/2\pi = \{0.05, 0.158, 0.0005, 26, 70, 10\}$ THz.

remarkable static dipoles. We have shown via full electrodynamic simulations that, when placed at the 50-nm gap between two closely spaced 1- μm -diameter spheres [46–48] of silicon carbide (SiC) [49], these dipoles provide couplings up to $\chi/2\pi = 0.1$ THz, with decay rates $\kappa/2\pi = 0.19$ THz (see Appendix G). Calculations on a nanoparticle-on-mirror geometry [50,51] of similar dimensions are also provided, yielding comparable light-matter coupling parameters. These calculations suggest that solid-state emitters with moderate static dipole moments—at least of the order of a few debyes—can reach interaction strengths comparable to those considered in this work. Such values of static dipole moments have been documented in various systems, including colloidal quantum dots [45], excitonic systems [52], perovskites [53], simple polar molecules [54], macromolecules [55], nonpolar molecules in matrices [56], NV centers [57], and Rydberg atoms [58].

Furthermore, it is worth noting that values different from those considered here could also potentially yield detectable emission of THz radiation. For a fixed cavity configuration, the minimum required value of \mathbf{d}_{ee} to achieve an output power that provides a signal-to-noise ratio (SNR) of one is a function of the noise-equivalent power (NEP) of the detectors used. We provide the exact relationship in Appendix H, where we confirm that the output flux provided by the emitters and cavities mentioned above can be detected by a variety of present-day THz detectors.

As a particular example, we can consider current superconducting THz detectors, that can achieve an NEP of up to 10^{-19} W Hz $^{-1/2}$ with responses below nanoseconds [59]. Together with the bandwidths here considered

(approximately 0.16 THz), these figures yield a minimum detectable power close to $P_{\min} = \text{NEP} \times \sqrt{\kappa} = 4 \cdot 10^{-14}$ W. Thus, even with a moderate output photon flux of $4 \cdot 10^{-4}$ THz [cf. Fig. 2(b)] and radiative decays κ^{rad} of 50% of the total decay rate ($\kappa = \kappa^{\text{rad}} + \kappa^{\text{abs}}$, κ^{abs} being the absorption rate in SiC), we can estimate an emitted power $P = \kappa^{\text{rad}} \langle \hat{X}^- \hat{X}^+ \rangle \hbar \omega_c \approx 6 \cdot 10^{-13}$ W. This estimation amounts to an SNR of roughly 10, which, together with future engineering of emitter interactions on nanostructures and further advances in material science, provides prospects for the creation of bright THz single-photon emitters. Furthermore, since we have shown that the brightness of our source is a function of the line width of the emitter, we expect that it could be further amplified via Purcell enhancement by adding a second cavity on resonance with the optical transition of the emitter.

The robustness against thermal noise is explored in Appendix I, where it is shown that the system could operate at temperatures corresponding to nitrogen cooling.

It is also important to consider the feasibility of experimentally measuring photon statistics and establishing the single-photon character of the source that we propose. This entails measurements of the second-order correlation function $g^{(2)}(\tau)$, which are typically done via time tagging in Hanbury Brown–Twiss setups [60]. The key figure of merit is the time resolution of the detectors, which need to resolve the intrinsic time scale of the correlations, τ_c . In our source, this time scale is given by $\tau_c \approx \left[(\gamma_- + \gamma_+) (1 + \tilde{C}) \right]^{-1}$ (see Fig. 14 in Appendix J), which is of the order of tenths of nanoseconds for the parameters considered here. The detection of correlations within this time scale can be readily achieved by state-of-the-art THz detectors with picosecond time resolution and a jitter time below 50 ps [61,62].

Further potential improvements to all these figures of merit could consist of enhanced nanophotonic architectures, such as hybrid cavities [63] or subwavelength waveguides [64], as well as the exploration of two-dimensional (2D) materials. These can provide THz nanocavities, such as 2D hexagonal boron nitride materials [65,66], as well as optically emitting defects [67].

VII. CONCLUSIONS

We have shown that a single coherently driven emitter with a permanent dipole moment in a THz cavity can operate as a versatile source of quantum THz radiation, accessing a broad range of frequencies and photon statistics and featuring a complex quantum correlations between different THz photons. The quantum sources that we propose call for exploring novel interfaces of optomechanical transductions of THz photons to optical ones [68–70], which, in conjunction with optical single-photon detectors or via single electron transistors [71], can open new avenues for

the detection of nonclassical THz correlations necessary to harvest the field of THz quantum optics. Beyond the immediate applications of single THz sources for technologies such as imaging or quantum communications, our findings represent a step toward future quantum technologies in the THz, which may consist of more complex cavity setups [64] capable of enhancing the multimode correlations that we identify here and turning them into integrated bright sources of entangled light [24,44] and matter [72] in the THz regime.

ACKNOWLEDGMENTS

This work makes use of the quantum toolbox in PYTHON (QuTiP) [73,74]. We acknowledge financial support from the Proyecto Sinérgico CAM 2020 Y2020/TCS-6545 (NanoQuCo-CM), and MCINN projects PID2021-126964OB-I00 (QENIGMA) and TED2021-130552B-C21 (ADIQUNANO). A.I.F.-D. acknowledges funding from the European Commission through the Europe Research and Innovation Programme under Agreement No. 101070700 (MIRAQLS). C.S.M. and D.M.C. also acknowledge the support of a fellowship from the Caixa Foundation (ID 100010434) and from the European Union Horizon 2020 research and innovation program under the Marie Skłodowska-Curie Grant Agreement No. 847648, with fellowship codes LCF/BQ/PI20/11760026 and LCF/BQ/PI20/11760018. D.M.C. also acknowledges support from the Ramon y Cajal program (RYC2020-029730-I). We thank Vincenzo Macrì for fruitful discussions.

APPENDIX A: DIFFERENCE BETWEEN THE STANDARD AND THE DRESSED MASTER EQUATION

Figure 5 shows that the choice of the master equation does not have any discernable impact on the results. Figure 6 shows the major difference that the change in the input-output relation makes. Note how in the resonances (especially $\Omega_R = \omega_c$), the deviation is negligible as long as κ is not too large. The largest discrepancy for $g^{(2)}(0)$ is found for $\Omega_R < \omega_c$.

APPENDIX B: ANALYTICAL EXPRESSIONS FOR THE JAYNES-CUMMINGS MODEL

In this appendix, we provide full analytical expressions obtained by solving the master equation with the Jaynes-Cummings Hamiltonian (i.e., with rotating-wave approximations applied), truncated at one cavity excitation. This truncation is justified by the very small numbers of cavity occupation that we obtain via exact numerical solutions of the master equation. The full expression for the cavity population that we obtain reads

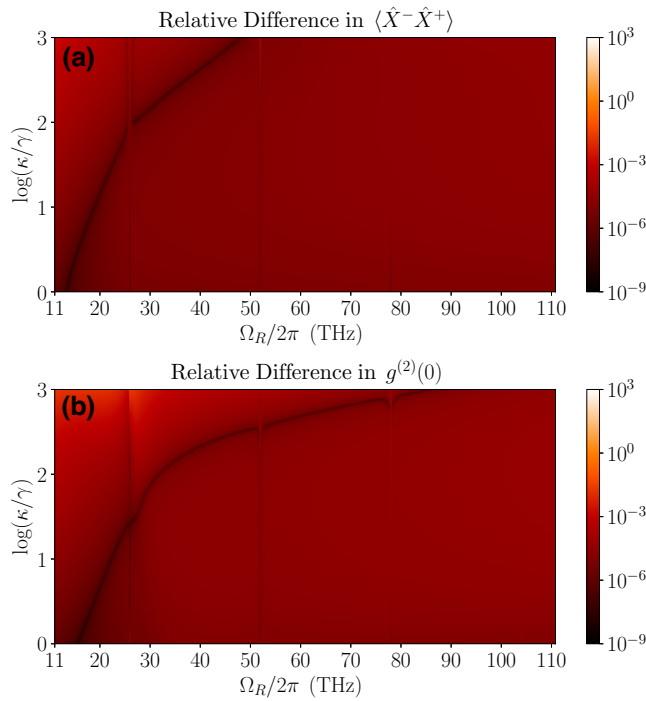


FIG. 5. Relative differences in expectation values between simulations using $\mathcal{D}(\hat{a})$ and $\mathcal{D}(\hat{X}^+)$: (a) relative difference in $\langle \hat{X}^- \hat{X}^+ \rangle$; (b) relative difference in $g^{(2)}(0)$.

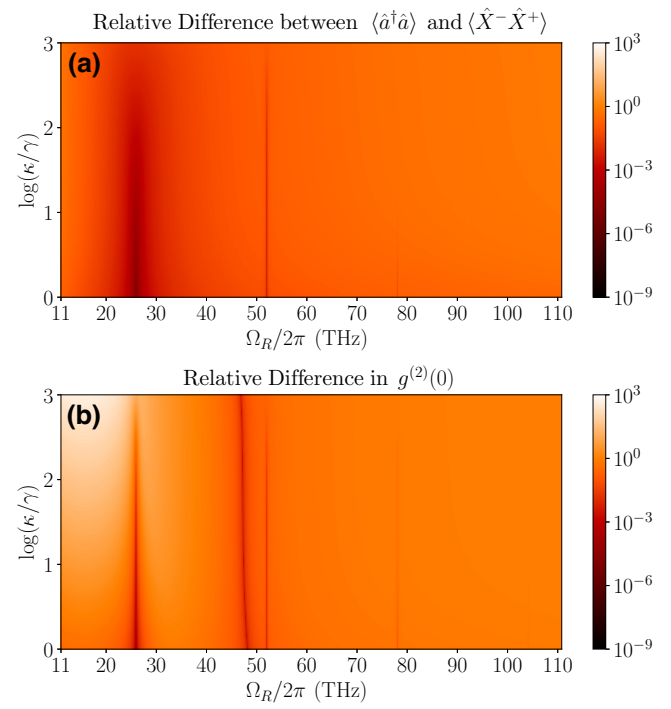


FIG. 6. Relative differences (a) between $\langle \hat{X}^- \hat{X}^+ \rangle$ and $\langle \hat{a}^\dagger \hat{a} \rangle$ and (b) between $\langle \hat{X}^- \hat{X}^- \hat{X}^+ \hat{X}^+ \rangle / \langle \hat{X}^- \hat{X}^+ \rangle^2$ and $\langle \hat{a}^\dagger \hat{a}^\dagger \hat{a} \hat{a} \rangle / \langle \hat{a}^\dagger \hat{a} \rangle^2$.

$$\langle \hat{a}^\dagger \hat{a} \rangle = \frac{16c^2 s^2 \chi^2 \gamma_+ \tilde{\kappa}}{16c^2 s^2 \chi^2 (\gamma_+ + \gamma_- + \kappa) \tilde{\kappa} + \kappa (\gamma_+ + \gamma_-) [4(\omega_c - \Omega_R)^2 + \tilde{\kappa}^2]}, \quad (\text{B1})$$

which describes a Lorentzian centered around $\Omega_R = \omega_c$. At resonance, $\Omega_R = \omega_c$, the expression of the steady-state population of the dressed quantum emitter is given by

$$\langle \hat{\xi}_+ \hat{\xi}_- \rangle = \frac{\gamma_+ [16c^2 s^2 \chi^2 + \kappa (\gamma_+ + \gamma_- + 4\gamma_z + \kappa)]}{16c^2 s^2 \chi^2 (\gamma_+ + \gamma_- + \kappa) + \kappa (\gamma_+ + \gamma_-) (\gamma_+ + \gamma_- + 4\gamma_z + \kappa)}, \quad (\text{B2})$$

which for $\gamma \ll \kappa$ simplifies to

$$\langle \hat{\xi}_+ \hat{\xi}_- \rangle = \frac{\gamma_+}{\gamma_+ + \gamma_-} \frac{1}{1 + \tilde{C}} = \frac{1}{1 + h^4} \frac{1}{1 + \tilde{C}}. \quad (\text{B3})$$

This exhibits population inversion when $h, \tilde{C} \ll 1$. In the limit $\tilde{C} \gg 1$, we have $\langle \hat{\xi}_+ \hat{\xi}_- \rangle \propto \tilde{C}^{-1}$, which signals a regime in which the dressed-emitter population is depleted via the efficient emission of THz photons through the cavity.

The exact formula for the maximum output flux for the optimum value of κ is

$$\max_{\kappa} [\kappa \langle \hat{a}^\dagger \hat{a} \rangle] = \frac{16c^2 s^2 \chi^2 \gamma_+}{(4cs\chi + \gamma_+ + \gamma_-)^2 + 4(\gamma_+ + \gamma_-)\gamma_z}. \quad (\text{B4})$$

In the limit $\chi \gg \gamma/4(c^4 + s^4)/sc$, the maximum flux is simply given by $\max_{\kappa} [\kappa \langle \hat{a}^\dagger \hat{a} \rangle] \approx \gamma_+$. Finally, a more general expression for the degree of quantum second-order coherence (from a model truncated at two cavity excitations), assuming $\gamma_-, \gamma_z \approx 0$, is given by

$$\begin{aligned}
g^{(2)}(0) = & 2(\gamma_+ + 2\kappa)[\gamma_+\kappa^2(\gamma_+ + \kappa)^2(\gamma_+ + 2\kappa)(\gamma_+ + 3\kappa) \\
& + 256c^4s^4\chi^4(\gamma_+^3 + 4\gamma_+\kappa + 12\gamma_+\kappa^2 + 6\kappa^3) \\
& + 16c^2s^2\chi^2\kappa(\gamma_+^4 + 5\gamma_+\kappa^3 + 17\gamma_+\kappa^2 \\
& + 23\gamma_+\kappa^3 + 6\kappa^4)] \\
& /[\kappa(\gamma_+ + \kappa)(\gamma_+ + 2\kappa)(\gamma_+ + 3\kappa) \\
& + 32c^2s^2\chi^2(\gamma_+^2 + 3\gamma_+\kappa + 3\kappa^2)]^2. \quad (B5)
\end{aligned}$$

APPENDIX C: MINIMUM LASER AMPLITUDES

In the limit $h \ll 1$, we require that $h \gg 1/\sqrt{4C}$ to maximize the flux. This is equivalent to demanding that $\Omega \gg \Omega_R/\sqrt{C}$ (assuming $C \gg 1$). The Rabi frequency generated by a Gaussian laser beam is $\Omega = \sqrt{4\eta P/(\pi w^2)}|\mathbf{d}_{eg}|/\hbar$, where η is the wave impedance, P the power, and w is the beam waist. With laser beams with a power of $P = 1$ mW focused at $w = 390 - 1500$ nm in solid immersion lenses (SILs) of high-NA objectives, as reported in Refs. [75,76],

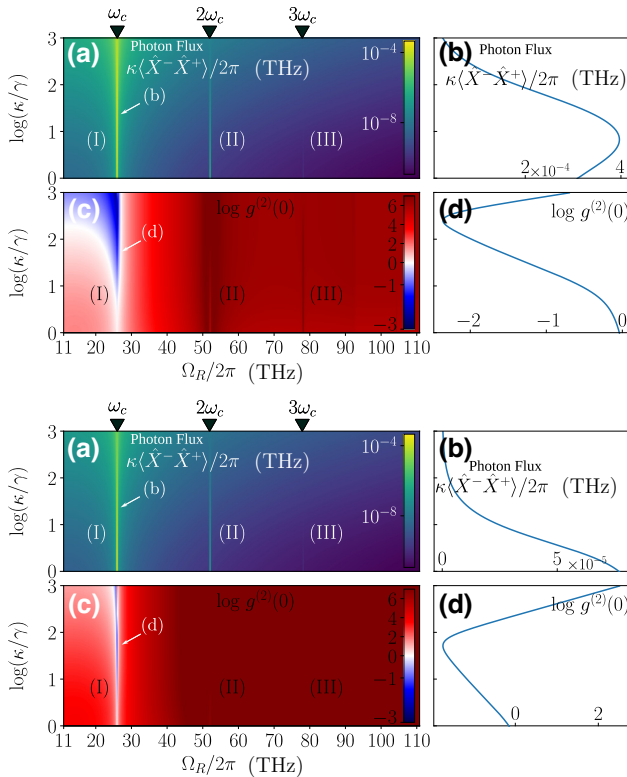


FIG. 7. Maps of (a) the output photon flux $\kappa\langle\hat{X}^-\hat{X}^+\rangle/2\pi$ (THz) and (c) the degree of quantum second-order coherence $g^{(2)}(0)$ [shown as $\log g^{(2)}(0)$] as a function of Ω_R for $\{\chi, \gamma, \omega_c\}/2\pi = \{0.05, 0.0005, 26\}$ THz for a fixed $\Delta/2\pi = 10$ THz, at a temperature of $T = 70$ K. (b),(d) The two adjunct plots show the scans of the maps shown in (a) and (c), respectively, along the resonance $\Omega_R = \omega_c$. The two figures represent $\Omega/2\pi = 1$ THz (top) and $\Omega/2\pi = 0.1$ THz (bottom), respectively.

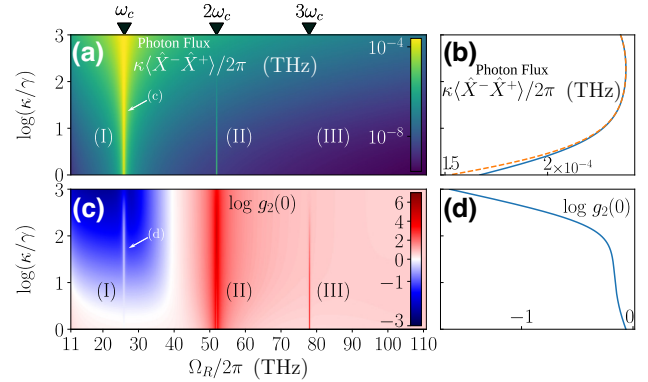


FIG. 8. Maps of (a) the output photon flux $\kappa\langle\hat{X}^-\hat{X}^+\rangle$ [shown as $\kappa\langle\hat{X}^-\hat{X}^+\rangle/2\pi$ (THz)] and (c) the degree of quantum second-order coherence $g^{(2)}(0)$ [shown as $\log g^{(2)}(0)$] as a function of Ω_R for $\{\chi, \gamma, \omega_c\}/2\pi = \{0.05, 0.0005, 26\}$ THz for a fixed $\Delta/2\pi = 10$ THz. (b),(d) The two adjunct plots show the scans of the maps along the resonance $\Omega_R = \omega_c$.

Rabi frequencies of the order of $10^3\gamma$ are within reach. Figure 7 shows the effect of choosing a lower laser coupling Ω . The antibunched region that we had for $\Omega_R < \omega_c$ is pushed back only until it is found in close vicinity to the resonance. In resonance, values of $g^{(2)}(0)$ close to 10^{-2} can still be reached. Lowering Ω too much, however, comes at a cost in brightness and smaller regions of antibunching in parameter space.

APPENDIX D: TUNABILITY VIA THE LASER AMPLITUDE

Here, we provide further information and results on the implications of modifying the Rabi frequency Ω_R by tuning the laser amplitude, rather than the laser frequency. Figure 8 is the analogue of Fig. 2, except that now Δ instead of Ω is kept constant, thus showing an alternative way to tune the quantum statistics with the laser amplitude. The results are similar, the main differences being an overall lower flux and a lower value of $g^{(2)}(0)$. Note that, in this situation, h is about 3 times larger here than in the main text. For instance, in the resonance (I), we obtain $h \approx 0.67$, in contrast to the value $h \approx 0.2$ corresponding to the results presented in the main text.

APPENDIX E: VALIDITY OF THE EFFECTIVE HAMILTONIAN

To check the validity of our assumption that at the specific points (II) and (III), the Hamiltonian is indeed dominated by terms proportional to $\lambda_n[(\hat{a})^n\hat{\zeta}_+ + (\hat{a}^\dagger)^n\hat{\zeta}_-]$, we compare the (Δ, Ω) -dependence of the effective coupling strengths λ_n , obtained via perturbation theory, with the n th Glauber correlation function $\langle(\hat{X}^-)^n(\hat{X}^+)^n\rangle$, which gives the probability of at least encountering n photons.

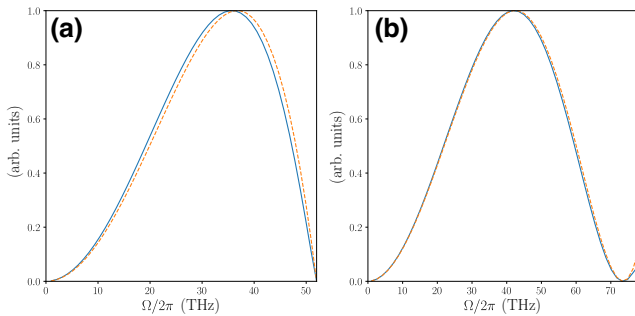


FIG. 9. Comparative plots of $|\lambda_n|^2$ (blue solid line) and $\langle (\hat{X}^-)^n (\hat{X}^+)^n \rangle$ (orange dashed line) for (a) $n = 2$ and (b) $n = 3$, for varying Ω and fixed $\Omega_R = n\omega_c$.

We have

$$\lambda_2 = \frac{\chi^2}{\omega_c^2} [cs(s^2 - c^2)] \quad (E1)$$

and

$$\lambda_3 = \frac{\chi^3}{\omega_c^2} [c^3 s^3 - 2cs(s^2 - c^2)^2]. \quad (E2)$$

As can be seen in Fig. 9, there is a good agreement between the effective two- and three-photon transition rates and the correlation functions at second and third order, respectively, validating our interpretation of the results at (II) and (III).

APPENDIX F: FILTERED PHOTON STATISTICS

Here, we elaborate on the numerical method employed for the calculation of frequency-filtered photon statistics. The calculation is done by coupling the system to two bosonic modes \hat{b}_i acting as sensors, with energy ω_i and line width $\Gamma = \kappa$. Resorting to the sensor method developed in Ref. [35], where the cavity mode is extremely weakly coupled ($\epsilon \ll \sqrt{\Gamma\gamma/2}$), $\hat{H}_c = \epsilon \sum_i (\hat{b}_i \hat{X}^- + \hat{b}_i^\dagger \hat{X}^+)$, we compute the spectrum and the frequency-resolved degree of quantum second-order coherence by computing expectation values of the sensors, yielding

$$S_\Gamma(\omega) = \lim_{\epsilon \rightarrow 0} \langle \hat{b}_1^\dagger \hat{b}_1 \rangle \quad (F1)$$

and

$$g_\Gamma^{(2)}(\omega_1, \omega_2) = \lim_{\epsilon \rightarrow 0} \frac{\langle \hat{b}_1^\dagger \hat{b}_1 \hat{b}_2^\dagger \hat{b}_2 \rangle}{\langle \hat{b}_1^\dagger \hat{b}_1 \rangle \langle \hat{b}_2^\dagger \hat{b}_2 \rangle}, \quad (F2)$$

respectively.

APPENDIX G: FULL ELECTRODYNAMIC SIMULATIONS OF A POTENTIAL THz CAVITY

We propose here a dimer of SiC microspheres as a potential platform for the realization of the THz cavity considered in our model. The frequency-dependent permittivity for this polar crystal, in the vicinity of the reststrahlen band, can be approximated by a Lorentz oscillator model

$$\epsilon_{\text{SiC}}(\omega) = \epsilon_\infty + \frac{\epsilon_\infty(\omega_{\text{LO}}^2 - \omega_{\text{TO}}^2)}{\omega_{\text{TO}}^2 - \omega^2 - i\omega\Gamma_{\text{SiC}}}, \quad (G1)$$

where $\omega_{\text{TO}}/2\pi = 23.61$ THz and $\omega_{\text{LO}}/2\pi = 28.91$ THz are the transverse and longitudinal optical phonon frequencies, $\Gamma_{\text{SiC}}/2\pi = 0.084$ THz is the absorption damping, and $\epsilon_\infty = 7$ is the static permittivity. These values are taken from the experimental fitting in Ref. [49], neglecting anisotropic effects in the SiC response.

The spectral density in Fig. 10(a) presents a number of peaks, originating from the surface-phonon-polariton resonances sustained by the cavity. This is defined in terms of the electromagnetic dyadic Green's function and the static dipole moment as $J(\omega) = \omega^2/(\pi\epsilon_0\hbar c^2)\mathbf{d}_{ee}\text{Im}\{\mathbf{G}(\mathbf{r}, \mathbf{r}, \omega)\}\mathbf{d}_{ee}$. It can be shown [47] that, in the quasistatic limit, it can be expressed as a sum of Lorentzian terms of the form

$$J(\omega) = \sum_n \frac{\chi_n^2}{\pi} \frac{\kappa_n/2}{(\omega - \omega_n)^2 + (\kappa_n/2)^2}, \quad (G2)$$

where χ_n is the electromagnetic coupling strength for mode n , ω_n its natural frequency, and Γ_n its damping rate (including both radiative and absorption channels).

Here, we will only focus on the two lowest-frequency modes ($n = 1, 2$), which have strong dipolar and quadrupolar characters, respectively. The inset of Fig. 10(a) demonstrates that only these two modes contribute significantly to the THz emission from the cavity (weighted by the radiative contribution to the total spectral density [48]). The surface-phononic resonances at higher-frequencies, and particularly the pseudomode at 28.25 THz, are dark, and remain effectively decoupled from the far field of the cavity. Through a Lorentzian fitting of the numerical $J(\omega)$, we can extract the parameters for these two modes (see Table I).

Note that we have split the mode damping rate, κ_n , into its radiative, κ_n^{rad} , and absorption components, and that the

TABLE I. The parameters of the two contributing modes for the dimer of SiC microspheres.

	$\omega_n/2\pi$ (THz)	$\kappa_n/2\pi$ (THz)	$\kappa_n^{\text{rad}}/2\pi$ (THz)	$\chi_n/2\pi$ (THz)
$n = 1$	26.815	0.186	0.101	0.102
$n = 2$	27.657	0.131	0.046	0.123

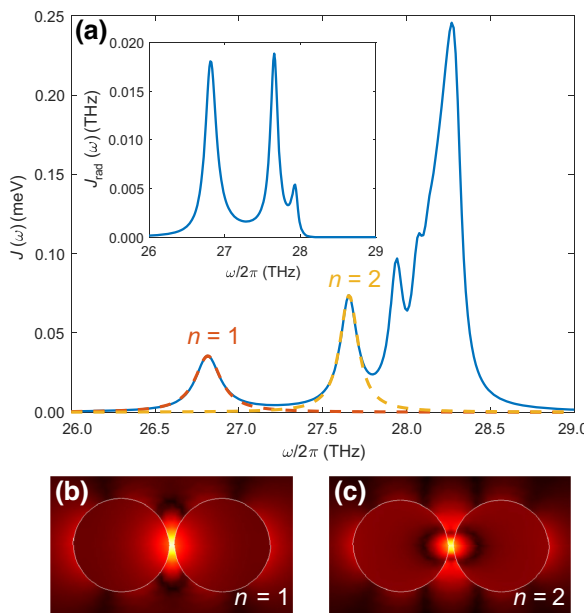


FIG. 10. (a) A plot of the spectral density, $J(\omega)$ [47], at the center of the 50-nm gap between two 1- μm -diameter SiC spheres. The emitter orientation is parallel to the dimer axis and we have taken $|\mathbf{d}_{ee}|=50$ D for its static dipole moment (also in accordance with experiments [45]). $J(\omega)$ has been obtained by means of full electrodynamic simulations using the finite-element solver of Maxwell's equations implemented in COMSOL MULTIPHYSICS. The inset shows the radiative spectral density for the cavity. (b),(c) Amplitude maps for the electric field component along the dimer axis and for the (b) $n = 1$ and (c) $n = 2$ surface phononic modes. The colors render the field amplitude in linear scale from black (minimum) to yellow (maximum).

latter is given by the loss in the SiC permittivity, $\kappa_n^{\text{abs}} = \Gamma_{\text{SiC}}$, i.e., $\kappa_n = \kappa_n^{\text{rad}} + \Gamma_{\text{SiC}}$. Figures 10(b) and 10(c) show maps of the electric field amplitude parallel to the emitter orientation (dimer axis) for the $n = 1$ and $n = 2$ surface-phononic modes, respectively.

In recent years, nanocube-on-mirror geometries have attracted attention in the context of plasmonic antennas. Their fabrication is simpler than the nanosphere dimer geometry in Fig. 10, as they are compatible with chemical-deposition techniques and their planar character makes them suitable for integration with other photonic components. Hoang *et al.* [50,51] have recently shown that their performance for ultrafast light generation can overcome nanosphere dimers. We explore this antenna architecture in Fig. 11. The system consists of a 1- μm SiC nanocube with chamfered edges and corners on top of a flat SiC substrate. The gap between them is 50 nm and the vertically oriented emitter is placed not at the geometrical center of the gap but displaced by 0.25 μm , which enables the excitation of a plasmonic mode with a net dipolar moment parallel to the SiC substrate and therefore directional emission in the vertical direction. Figure 11(a) plots

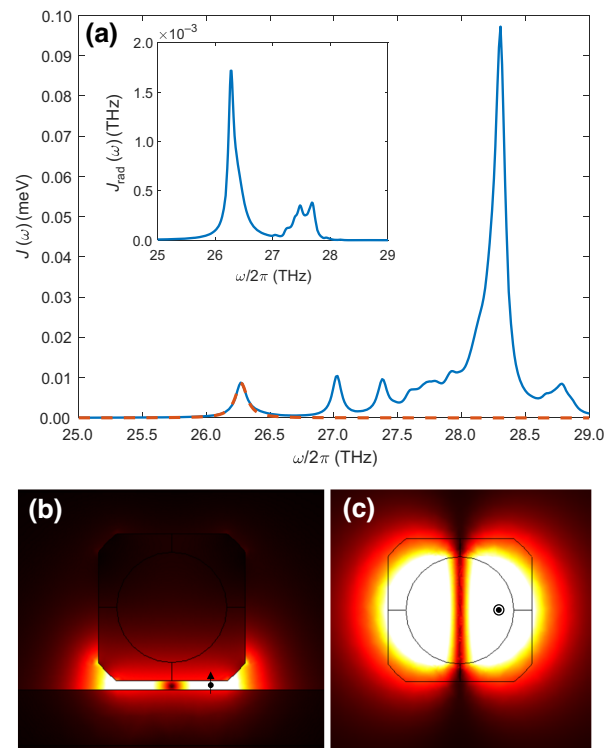


FIG. 11. (a) A plot of the spectral density, $J(\omega)$, at the 50 nm gap between a 1- μm side-chamfered SiC nanocube and a flat SiC substrate. The emitter orientation is vertical and its in-plane position is displaced by 0.25 μm from the geometrical center (see black arrows in the panels below). As in Fig. 10, we have taken $|\mathbf{d}_{ee}| = 50$ D for its static dipole moment. The inset renders the radiative spectral density for the same configuration and shows that only the lowest radiative mode contributes significantly to the far-field signal, with an efficiency of approximately 22%. (b),(c) Electric field amplitude maps for this mode in two different cross sections of the structure. The black dots indicate the emitter position and the black arrow in (b) its orientation. The colors render the field amplitude in linear scale from black (minimum) to yellow (maximum).

the spectral density for this geometry and the same static dipole moment as in Fig. 10. We can observe that the lowest brightest mode sustained by the geometry is in the same window as the nanosphere dimer but the inset shows that this lowest-energy mode is the only that radiates efficiently out of the structure. Figures 11(b) and 11(c) display electric field amplitude maps for this mode within two different cross sections of the structure. The black dots indicate the emitter position and the black arrow in Fig. 11(b) its orientation. The Lorentzian fitting to $J(\omega)$ for this mode yields $\omega_1/2\pi = 26.27$ THz, $\kappa_1/2\pi = 0.11$ THz, $\kappa_1^{\text{rad}}/2\pi = 0.028$ THz, and $\chi_1/2\pi = 0.040$ THz. These values are similar to those obtained for the microspheres in Table I.

APPENDIX H: POTENTIAL EXPERIMENTAL PARAMETERS

Here, we show the relationship between a given detector NEP and the permanent dipole moment that is required to reach a detectable flux, i.e., yielding an SNR equal to 1. These results have been obtained by equating the output power

$$P = \hbar\omega_c \kappa^{\text{rad}} \langle \hat{X}^- \hat{X}^+ \rangle \approx \hbar\omega_c \frac{\kappa}{\tilde{C}} \left(\frac{\gamma_+}{1 + \tilde{C}^{-1} - \frac{4\gamma_-}{\kappa}} \right), \quad (\text{H1})$$

with the minimum detectable power

$$P_{\min} = \text{NEP} \sqrt{\kappa}, \quad (\text{H2})$$

and solving for $|\mathbf{d}_{ee}|$ —which appears in \tilde{C} in the form of the coupling rate χ —essentially demanding an SNR of 1. Here, we have assumed that we are in the resonant regime $\Omega_R = \omega_c$ and that $\omega_c \gg \chi$, so that we are in the Jaynes-Cummings regime in which we can substitute \hat{X}^+ by \hat{a} in the calculation of the flux and we can make use of the analytical equations shown in the main text. Also, for simplicity, we consider here that the decay of the cavity is completely radiative ($\kappa = \kappa^{\text{rad}}$) and that the detector bandwidth is equal to κ .

We solve $P/P_{\min} = 1$ for $|\mathbf{d}_{ee}|$, while assuming that the permanent dipole can be related to the coupling rate χ by extrapolating the full electrodynamical simulations, i.e., setting $|\mathbf{d}_{ee}| = \chi \cdot (50 \text{ D})/(0.1 \text{ THz})$. Figure 12 shows the values for $|\mathbf{d}_{ee}|$ and the NEP for which $P/P_{\min} = 1$. The highlighted spaces above the colored lines are the regions where a certain emitter-detector pair could feasibly produce a measurable outcome. Here, we have assumed that the emitter frequency is $\omega_0/2\pi = 400 \text{ THz}$ and $\kappa/2\pi = 0.158 \text{ THz}$. According to Eq. (2), when the permanent dipole is small, the output power is proportional to the cooperativity $\kappa \langle \hat{a}^\dagger \hat{a} \rangle = \gamma_+ \tilde{C}$ (or the square of the permanent dipole moment), which corresponds to the quadratic dependence shown at lower values of the NEP. When the permanent dipole moment is large, the output power plateaus at γ_+ , and it is thus mainly set by the optical spontaneous emission rate γ . For very large $|\mathbf{d}_{ee}|$, however, γ might become larger than κ , which will result in Eq. (2) becoming equal to $\kappa \tilde{C}$ for low $|\mathbf{d}_{ee}|$ and κ for large $|\mathbf{d}_{ee}|$ (see the blue line, with slightly different behavior).

Figure 12 shows that there are several realistic candidates for experimental implementation; e.g., a combination of quantum dots for the emitters and superconducting and/or single-electron devices for the detection seems like a conservative choice.

APPENDIX I: THERMAL EMISSION

We envisage that the system would operate at cryogenic temperatures of $T = 70 \text{ K}$, which corresponds roughly

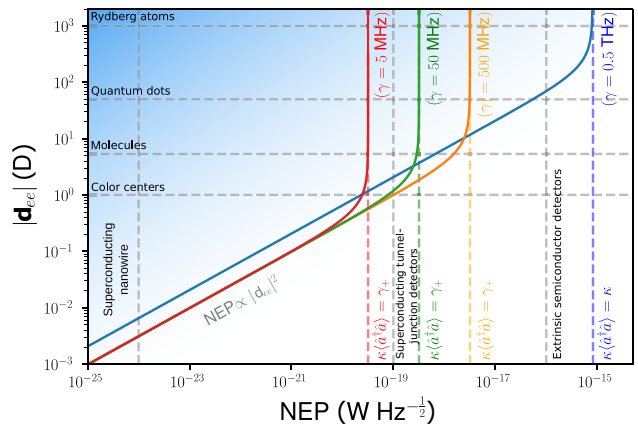


FIG. 12. A plot of the critical values of the noise-equivalent power (NEP) and permanent dipole moment, for which the system reaches a SNR of 1 in relation to different detectors and/or experimental realizations. The different curves correspond to different transition dipole moments and/or spontaneous emission rates [$\gamma = 5 \text{ MHz}$ (red), 50 MHz (green), 500 MHz (orange), and 0.5 THz (blue)]. The horizontal gray lines correspond to (from top to bottom) Cs Rydberg atoms [58], colloidal semiconductor nanocrystals [45], molecules [54,56], and diamond color centers [57]. The vertical gray lines correspond to (from left to right) superconducting nanowires [77], single-electron devices [78], and doped Si-Ge detectors [79]. The NEP for superconducting nanowires has been estimated via $\text{NEP} = \hbar\omega_c \sqrt{S}$ [68,80], where S is the dark-count rate.

to nitrogen cooling. For that temperature, the thermal-occupation number is $\langle n \rangle_{\text{th}} = (e^{\hbar\omega_c/k_B T} - 1)^{-1} \approx 10^{-8}$, while the cavity photon number in resonance (the regime that provides antibunching) is roughly 10^{-2} , meaning that neglecting thermal emission is justified in this regime. Figure 13 shows a simulation with added thermal emission in the cavity for $T = 70 \text{ K}$ with no qualitative difference from the plot at $T = 0 \text{ K}$ in the paper (except for a decrease in $g^{(2)}(0)$ for large Ω_R). At around $T = 200 \text{ K}$, the different features in the map of the quantum second-order coherence are almost completely gone and all that remains are thermal states, so room-temperature applications are unlikely.

APPENDIX J: TIME-DEPENDENT DEGREE OF QUANTUM SECOND-ORDER COHERENCE

When the cavity can be adiabatically eliminated, the dressed emitter is effectively described as a TLS under an incoherent pump, with rate γ_+ , and spontaneous emission modified by the cavity, with rate $\gamma_- + (\gamma_- + \gamma_+) \tilde{C}$. In that case, the second-order correlation function can be obtained analytically and is given by

$$g^{(2)}(\tau) = 1 - \exp \left[-(\gamma_+ + \gamma_-)(1 + \tilde{C})\tau \right]. \quad (\text{J1})$$

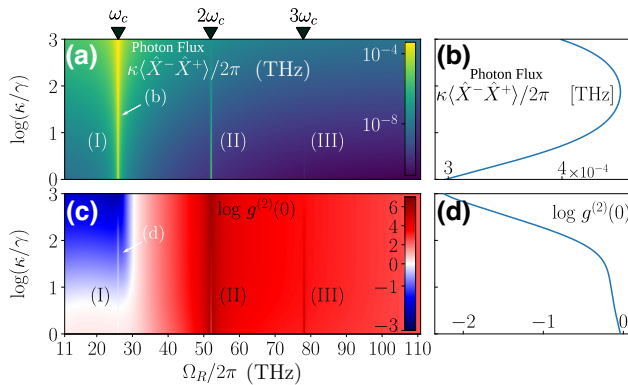


FIG. 13. Maps of (a) the output photon flux $\kappa \langle \hat{X}^- \hat{X}^+ \rangle$ [shown as $\kappa \langle \hat{X}^- \hat{X}^+ \rangle / 2\pi$ (THz)] and (c) the degree of quantum second-order coherence $g^{(2)}(0)$ [shown as $\log g^{(2)}(0)$] as a function of Ω_R for $\{\chi, \gamma, \omega_c\}/2\pi = \{0.05, 0.0005, 26\}$ THz for a fixed $\Delta/2\pi = 10$ THz, at a temperature of $T = 70$ K. (b),(d) The two adjunct plots show the scans of the maps shown in (a) and (c), respectively, along the resonance $\Omega_R = \omega_c$.

This equation establishes a correlation time scale given by

$$\tau_c = \left[(\gamma_+ + \gamma_-)(1 + \tilde{C}) \right]^{-1}. \quad (J2)$$

We have computed numerically the exact values of $g^{(2)}(\tau)$ without any approximations, shown in Fig. 14. The results, which are reasonably well approximated by the previous equation, confirm that the time delay between subsequent THz emissions is given by τ_c and sets its value to be of the order of 100 ps.

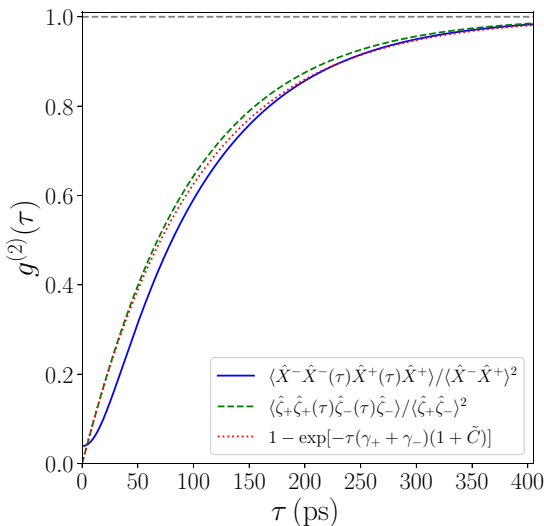


FIG. 14. The degree of quantum second-order coherence $g^{(2)}(\tau)$ of the cavity and the emitter as a function of time with an exponential fit. The parameters used are $\{\chi, \kappa, \gamma, \omega_c, \Omega_R, \Omega\}/2\pi = \{0.05, 0.158, 0.0005, 26, 26, 10\}$ THz.

- [1] M. Tonouchi, Cutting-edge terahertz technology, *Nat. Photonics* **1**, 97 (2007).
- [2] X. C. Zhang, A. Shkurinov, and Y. Zhang, Extreme terahertz science, *Nat. Photonics* **11**, 16 (2017).
- [3] N. Nagai, R. Kumazawa, and R. Fukasawa, Direct evidence of inter-molecular vibrations by THz spectroscopy, *Chem. Phys. Lett.* **413**, 495 (2005).
- [4] S. Nashima, O. Morikawa, K. Takata, and M. Hangyo, Temperature dependence of optical and electronic properties of moderately doped silicon at terahertz frequencies, *J. Appl. Phys.* **90**, 837 (2001).
- [5] L. Afsah-Hejri, P. Hajeb, P. Ara, and R. J. Ehsani, A comprehensive review on food applications of terahertz spectroscopy and imaging, *Compr. Rev. Food Sci. Food Saf.* **18**, 1563 (2019).
- [6] R. M. Woodward, B. E. Cole, V. P. Wallace, R. J. Pye, D. D. Arnone, E. H. Linfield, and M. Pepper, Terahertz pulse imaging in reflection geometry of human skin cancer and skin tissue, *Phys. Med. Biol.* **47**, 3853 (2002).
- [7] A. Hirata, T. Kosugi, H. Takahashi, R. Yamaguchi, F. Nakajima, T. Furuta, H. Ito, H. Sugahara, Y. Sato, and T. Nagatsuma, 120-GHz-band millimeter-wave photonic wireless link for 10-Gb/s data transmission, *IEEE Trans. Microw. Theory Tech.* **54**, 1937 (2006).
- [8] K. Kawase, Y. Ogawa, Y. Watanabe, and H. Inoue, Non-destructive terahertz imaging of illicit drugs using spectral fingerprints, *Opt. Express* **11**, 2549 (2003).
- [9] I. A. Walmsley, Quantum optics: Science and technology in a new light, *Science (New York)* **348**, 525 (2015).
- [10] X. Gu, A. F. Kockum, A. Miranowicz, Y.-x. Liu, and F. Nori, Microwave photonics with superconducting quantum circuits, *Phys. Rep.* **718–719**, 1 (2017).
- [11] A. Blais, A. L. Grimsmo, S. M. Girvin, and A. Wallraff, Circuit quantum electrodynamics, *Rev. Mod. Phys.* **93**, 025005 (2021).
- [12] J. Aasi, J. Abadie, B. Abbott, R. Abbott, T. Abbott, M. Abernathy, C. Adams, T. Adams, P. Addesso, and R. Adhikari *et al.*, Enhanced sensitivity of the LIGO gravitational wave detector by using squeezed states of light, *Nat. Photonics* **7**, 613 (2013).
- [13] M. H. Michael, M. Silveri, R. T. Brierley, V. V. Albert, J. Salmilehto, L. Jiang, and S. M. Girvin, New class of quantum error-correcting codes for a bosonic mode, *Phys. Rev. X* **6**, 031006 (2016).
- [14] D. Gottesman, H.-K. Lo, N. Lutkenhaus, and J. Preskill, in *International Symposium on Information Theory, 2004. ISIT 2004. Proceedings.* (IEEE, Chicago, IL, USA, 2004), p. 136.
- [15] B. E. Cole, J. B. Williams, B. T. King, M. S. Sherwin, and C. R. Stanley, Coherent manipulation of semiconductor quantum bits with terahertz radiation, *Nature* **410**, 60 (2001).
- [16] G. Kh. Kitaeva, V. V. Kornienko, A. A. Leontyev, and A. V. Shepelev, Generation of optical signal and terahertz idler photons by spontaneous parametric down-conversion, *Phys. Rev. A* **98**, 063844 (2018).
- [17] O. V. Kibis, G. Y. Slepyan, S. A. Maksimenko, and A. Hoffmann, Matter coupling to strong electromagnetic fields in two-level quantum systems with broken inversion symmetry, *Phys. Rev. Lett.* **102**, 023601 (2009).

- [18] I. G. Savenko, O. V. Kibis, and I. A. Shelykh, Asymmetric quantum dot in a microcavity as a nonlinear optical element, *Phys. Rev. A* **85**, 053818 (2012).
- [19] N. Shammah, C. C. Phillips, and S. De Liberato, Terahertz emission from ac Stark-split asymmetric intersubband transitions, *Phys. Rev. B* **89**, 235309 (2014).
- [20] I. Y. Chestnov, V. A. Shahnazaryan, A. P. Alodjants, and I. A. Shelykh, Terahertz lasing in ensemble of asymmetric quantum dots, *ACS Photonics* **4**, 2726 (2017).
- [21] S. De Liberato, Lasing from dressed dots, *Nat. Photonics* **12**, 4 (2018).
- [22] R. Pompe, M. Hensen, M. Otten, S. K. Gray, and W. Pfeiffer, Pure dephasing induced single-photon parametric down-conversion in a strongly coupled plasmon-exciton system, *Phys. Rev. B* **108**, 115432 (2023).
- [23] G. Oelsner, P. Macha, O. V. Astafiev, E. Il'ichev, M. Grajcar, U. Hübner, B. I. Ivanov, P. Neilinger, and H.-G. Meyer, Dressed-state amplification by a single superconducting qubit, *Phys. Rev. Lett.* **110**, 053602 (2013).
- [24] C. Sánchez Muñoz, F. P. Laussy, E. del Valle, C. Tejedor, and A. González-Tudela, Filtering multiphoton emission from state-of-the-art cavity quantum electrodynamics, *Optica* **5**, 14 (2018).
- [25] F. Beaudoin, J. M. Gambetta, and A. Blais, Dissipation and ultrastrong coupling in circuit QED, *Phys. Rev. A* **84**, 043832 (2011).
- [26] A. Settineri, V. Macrì, A. Ridolfo, O. Di Stefano, A. F. Kockum, F. Nori, and S. Savasta, Dissipation and thermal noise in hybrid quantum systems in the ultrastrong-coupling regime, *Phys. Rev. A* **98**, 053834 (2018).
- [27] M. Lednev, F. J. García-Vidal, and J. Feist, A Lindblad master equation capable of describing hybrid quantum systems in the ultra-strong coupling regime, arXiv preprint [arXiv:2305.13171](https://arxiv.org/abs/2305.13171) (2023).
- [28] A. Ridolfo, M. Leib, S. Savasta, and M. J. Hartmann, Photon blockade in the ultrastrong coupling regime, *Phys. Rev. Lett.* **109**, 193602 (2012).
- [29] H. Carmichael, *An Open Systems Approach to Quantum Optics: Lectures Presented at the Université Libre de Bruxelles, October 28 to November 4, 1991* (Springer Science & Business Media, Brussels, Belgium, 2009), Vol. 18.
- [30] K. K. W. Ma and C. K. Law, Three-photon resonance and adiabatic passage in the large-detuning Rabi model, *Phys. Rev. A* **92**, 023842 (2015).
- [31] O. Di Stefano, A. F. Kockum, A. Ridolfo, S. Savasta, and F. Nori, Photodetection probability in quantum systems with arbitrarily strong light-matter interaction, *Sci. Rep.* **8**, 17825 (2018).
- [32] L. Garziano, R. Stassi, V. Macrì, A. F. Kockum, S. Savasta, and F. Nori, Multiphoton quantum Rabi oscillations in ultrastrong cavity QED, *Phys. Rev. A* **92**, 063830 (2015).
- [33] L. Garziano, V. Macrì, R. Stassi, O. Di Stefano, F. Nori, and S. Savasta, One photon can simultaneously excite two or more atoms, *Phys. Rev. Lett.* **117**, 043601 (2016).
- [34] C. Sánchez Muñoz, A. Frisk Kockum, A. Miranowicz, and F. Nori, Simulating ultrastrong-coupling processes breaking parity conservation in Jaynes-Cummings systems, *Phys. Rev. A* **102**, 033716 (2020).
- [35] E. del Valle, A. Gonzalez-Tudela, F. P. Laussy, C. Tejedor, and M. J. Hartmann, Theory of frequency-filtered and time-resolved $\$N\$$ -photon correlations, *Phys. Rev. Lett.* **109**, 183601 (2012).
- [36] A. Gonzalez-Tudela, F. P. Laussy, C. Tejedor, M. J. Hartmann, and E. del Valle, Two-photon spectra of quantum emitters, *New J. Phys.* **15**, 033036 (2013).
- [37] A. Ulhaq, S. Weiler, S. M. Ulrich, R. Roßbach, M. Jetter, and P. Michler, Cascaded single-photon emission from the Mollow triplet sidebands of a quantum dot, *Nat. Photonics* **6**, 238 (2012).
- [38] R. Horodecki, P. Horodecki, M. Horodecki, and K. Horodecki, Quantum entanglement, *Rev. Mod. Phys.* **81**, 865 (2009).
- [39] H. J. Kimble, The quantum Internet, *Nature* **453**, 1023 (2008).
- [40] R. Loudon, Non-classical effects in the statistical properties of light, *Rep. Prog. Phys.* **43**, 913 (1980).
- [41] C. Sánchez Muñoz, E. del Valle, C. Tejedor, and F. P. Laussy, Violation of classical inequalities by photon frequency filtering, *Phys. Rev. A* **90**, 052111 (2014).
- [42] M. Peiris, B. Petrak, K. Konthasinghe, Y. Yu, Z. C. Niu, and A. Müller, Two-color photon correlations of the light scattered by a quantum dot, *Phys. Rev. B* **91**, 195125 (2015).
- [43] J. F. Clauser, M. A. Horne, A. Shimony, and R. A. Holt, Proposed experiment to test local hidden-variable theories, *Phys. Rev. Lett.* **23**, 880 (1969).
- [44] C. Sánchez Muñoz, E. del Valle, A. G. Tudela, K. Müller, S. Lichtmannecker, M. Kaniber, C. Tejedor, J. J. Finley, and F. P. Laussy, Emitters of N -photon bundles, *Nat. Photonics* **8**, 550 (2014).
- [45] M. Shim and P. Guyot-Sionnest, Permanent dipole moment and charges in colloidal semiconductor quantum dots, *J. Chem. Phys.* **111**, 6955 (1999).
- [46] R. Sáez-Blázquez, Á. Cuartero-González, J. Feist, F. J. García-Vidal, and A. I. Fernández-Domínguez, Plexcitonic quantum light emission from nanoparticle-on-mirror cavities, *Nano Lett.* **22**, 2365 (2022).
- [47] R.-Q. Li, D. Hernández-Pérez, F. J. García-Vidal, and A. I. Fernández-Domínguez, Transformation optics approach to plasmon-exciton strong coupling in nanocavities, *Phys. Rev. Lett.* **117**, 107401 (2016).
- [48] D. Zhao, R. E. F. Silva, C. Climent, J. Feist, A. I. Fernández-Domínguez, and F. J. García-Vidal, Impact of vibrational modes in the plasmonic Purcell effect of organic molecules, *ACS Photonics* **7**, 3369 (2020).
- [49] T. E. Tiwald, J. A. Woollam, S. Zollner, J. Christiansen, R. B. Gregory, T. Wetteroth, S. R. Wilson, and A. R. Powell, Carrier concentration and lattice absorption in bulk and epitaxial silicon carbide determined using infrared ellipsometry, *Phys. Rev. B* **60**, 11464 (1999).
- [50] T. B. Hoang, G. M. Akselrod, C. Argyropoulos, J. Huang, D. R. Smith, and M. H. Mikkelsen, Ultrafast spontaneous emission source using plasmonic nanoantennas, *Nat. Commun.* **6**, 7788 (2015).
- [51] T. B. Hoang, G. M. Akselrod, and M. H. Mikkelsen, Ultrafast room-temperature single photon emission from quantum dots coupled to plasmonic nanocavities, *Nano Lett.* **16**, 270 (2016).

- [52] R. Rapaport, G. Chen, and S. H. Simon, Nonlinear dynamics of a dense two-dimensional dipolar exciton gas, *Phys. Rev. B* **73**, 033319 (2006).
- [53] B. Lv, T. Zhu, Y. Tang, Y. Lv, C. Zhang, X. Wang, D. Shu, and M. Xiao, Probing permanent dipole moments and removing exciton fine structures in single perovskite nanocrystals by an electric field, *Phys. Rev. Lett.* **126**, 197403 (2021).
- [54] J. Deiglmayr, A. Grochola, M. Repp, O. Dulieu, R. Wester, and M. Weidmüller, Permanent dipole moment of LiCs in the ground state, *Phys. Rev. A* **82**, 032503 (2010).
- [55] V. A. Kovarskii, Quantum processes in biological molecules. Enzyme catalysis, *Physics—Uspekhi* **42**, 797 (1999).
- [56] A. Moradi, Z. Ristanović, M. Orrit, I. Deperasinska, and B. Kozankiewicz, Matrix-induced linear Stark effect of single dibenzoterrylene molecules in 2,3-dibromonaphthalene crystal, *ChemPhysChem* **20**, 55 (2019).
- [57] P. Tamarat, T. Gaebel, J. R. Rabeau, M. Khan, A. D. Green-tree, H. Wilson, L. C. L. Hollenberg, S. Prawer, P. Hemmer, F. Jelezko, and J. Wrachtrup, Stark shift control of single optical centers in diamond, *Phys. Rev. Lett.* **97**, 083002 (2006).
- [58] D. Booth, S. T. Rittenhouse, J. Yang, H. R. Sadeghpour, and J. P. Shaffer, Production of trilobite Rydberg molecule dimers with kilo-Debye permanent electric dipole moments, *Science* **348**, 99 (2015).
- [59] F. Sizov, Terahertz radiation detectors: The state-of-the-art, *Semicond. Sci. Technol.* **33**, 123001 (2018).
- [60] N. Somaschi, V. Giesz, L. De Santis, J. C. Loredo, M. P. Almeida, G. Hornecker, S. L. Portalupi, T. Grange, C. Antón, J. Demory, C. Gómez, I. Sagnes, N. D. Lanzillotti-Kimura, A. Lemaître, A. Aufjeves, A. G. White, L. Lanco, and P. Senellart, Near-optimal single-photon sources in the solid state, *Nat. Photonics* **10**, 340 (2016).
- [61] M. Loidolt-Krüger, F. Jolmes, M. Patting, M. Wahl, E. Sismakis, A. Devaux, U. Ortmann, F. Koberling, and R. Erdmann, Visualizing dynamic processes with rapid-FLIMHiRes, the ultra fast FLIM imaging method with outstanding 10ps time resolution, *Spie Eco-Photonics 2011: Sustainable Design, Manufacturing, and Engineering Workforce Education for A Green Future* **11648**, 116480D (2021).
- [62] M. Caselle, M. Balzer, S. Chilingaryan, M. Hofherr, V. Judin, A. Kopmann, N. J. Smale, P. Thoma, S. Wuensch, A.-S. Müller, M. Siegel, and M. Weber, An ultra-fast data acquisition system for coherent synchrotron radiation with terahertz detectors, *J. Instrum.* **9**, C01024 (2014).
- [63] B. Gurlek, V. Sandoghdar, and D. Martín-Cano, Manipulation of quenching in nanoantenna-emitter systems enabled by external detuned cavities: A path to enhance strong-coupling, *ACS Photonics* **5**, 456 (2017).
- [64] D. Martín-Cano, M. L. Nesterov, A. I. Fernandez-Dominguez, F. J. Garcia-Vidal, L. Martín-Moreno, and E. Moreno, Domino plasmons for subwavelength terahertz circuitry, *Opt. Express* **18**, 754 (2010).
- [65] M. Autore, P. Li, I. Dolado, F. J. Alfaro-Mozaz, R. Esteban, A. Atxabal, F. Casanova, L. E. Hueso, P. Alonso-González, J. Aizpurua, A. Y. Nikitin, S. Vélez, and R. Hillenbrand, Boron nitride nanoresonators for phonon-enhanced molecular vibrational spectroscopy at the strong coupling limit, *Light: Sci. Appl.* **7**, 17172 (2018).
- [66] J. D. Caldwell, I. Aharonovich, G. Cassabois, J. H. Edgar, B. Gil, and D. N. Basov, Photonics with hexagonal boron nitride, *Nat. Rev. Mater.* **4**, 552 (2019).
- [67] Y. Xia, Q. Li, J. Kim, W. Bao, C. Gong, S. Yang, Y. Wang, and X. Zhang, Room-temperature giant Stark effect of single photon emitter in van der Waals material, *Nano Lett.* **19**, 7100 (2019).
- [68] P. Roelli, D. Martin-Cano, T. J. Kippenberg, and C. Galland, Molecular platform for frequency upconversion at the single-photon level, *Phys. Rev. X* **10**, 031057 (2020).
- [69] A. Xomalis, X. Zheng, R. Chikkaraddy, Z. Koczor-Benda, E. Miele, E. Rosta, G. A. E. Vandembosch, A. Martínez, and J. J. Baumberg, Detecting mid-infrared light by molecular frequency upconversion in dual-wavelength nanoantennas, *Science (New York)* **374**, 1268 (2021).
- [70] W. Chen, P. Roelli, H. Hu, S. Verlekar, S. P. Amirtharaj, A. I. Barreda, T. J. Kippenberg, M. Kovylina, E. Verhagen, A. Martínez, and C. Galland, Continuous-wave frequency upconversion with a molecular optomechanical nanocavity, *Science (New York)* **374**, 1264 (2021).
- [71] S. Komiyama, O. Astafiev, V. Antonov, T. Kutsuwa, and H. Hirai, A single-photon detector in the far-infrared range, *Nature* **403**, 405 (2000).
- [72] A. Gonzalez-Tudela, D. Martín-Cano, E. Moreno, L. Martín-Moreno, C. Tejedor, and F. J. García-Vidal, Entanglement of two qubits mediated by one-dimensional plasmonic waveguides, *Phys. Rev. Lett.* **106**, 020501 (2011).
- [73] J. R. Johansson, P. D. Nation, and F. Nori, QuTiP: An open-source PYTHON framework for the dynamics of open quantum systems, *Comput. Phys. Commun.* **183**, 1760 (2012).
- [74] J. R. Johansson, P. D. Nation, and F. Nori, QuTiP 2: A PYTHON framework for the dynamics of open quantum systems, *Comput. Phys. Commun.* **184**, 1234 (2013).
- [75] M. Colautti, F. S. Piccioli, Z. Ristanović, P. Lombardi, A. Moradi, S. Adhikari, I. Deperasinska, B. Kozankiewicz, M. Orrit, and C. Toninelli, Laser-induced frequency tuning of Fourier-limited single-molecule emitters, *ACS Nano* **14**, 13584 (2020).
- [76] C. Lange, E. Daggett, V. Walther, L. Huang, and J. D. Hood, Superradiant and subradiant states in lifetime-limited organic molecules through laser-induced tuning, *arxiv:2308.08037* [quant-ph] (2023).
- [77] V. B. Verma, B. Korzh, A. B. Walter, A. E. Lita, R. M. Briggs, M. Colangelo, Y. Zhai, E. E. Wollman, A. D. Beyer, J. P. Allmaras, H. Vora, D. Zhu, E. Schmidt, A. G. Kozorezov, K. K. Berggren, R. P. Mirin, S. W. Nam, and M. D. Shaw, Single-photon detection in the mid-infrared up to 10 μm wavelength using tungsten silicide superconducting nanowire detectors, *APL Photonics* **6**, 056101 (2021).
- [78] R. Schoelkopf, S. Moseley, C. Stahle, P. Wahlgren, and P. Delsing, A concept for a submillimeter-wave single-photon counter, *IEEE Trans. Appl. Supercond.* **9**, 2935 (1999).
- [79] N. Sclar, Properties of doped silicon and germanium infrared detectors, *Prog. Quantum Electron.* **9**, 149 (1984).
- [80] R. H. Hadfield, Single-photon detectors for optical quantum information applications, *Nat. Photonics* **3**, 696 (2009).